

Tailoring the Electrocatalytic Properties of Novel Microwave synthesized $\text{CuNd}_{(2-x)}\text{Gd}_x\text{O}_4$ Nanoparticles for Efficient Total Water Splitting in Alkaline Media

Anto Priyanka E,^a Sreenivasan Nagappan,^{b,c} J. Judith Vijaya,^{a,*} Angappan Sankaramahalingam^c and Subrata Kundu^{b, c, *}

^a *Catalysis and Nanomaterials Research Laboratory, Department of Chemistry, Loyola College, Chennai 600 034, Tamil Nadu, India.*

^b *Academy of Scientific and Innovative Research (AcSIR), Ghaziabad-201002, India.*

^c *Electrochemical Process Engineering (EPE) Division, CSIR-Central Electrochemical Research Institute (CECRI), Karaikudi-630003, Tamil Nadu, India.*

*To whom correspondence should be addressed,

E-mail: jjvijaya78@gmail.com; judithvijaya@loyolacollege.edu; Phone: (+91) 9500026204

E-mail: skundu@cecri.res.in; kundu.subrata@gmail.com, Phone: (+ 91) 4565-241487.

Supplementary information for this article is given via a link at the end of the document

This file contains 22 pages in which the details of Materials and electrochemical characterizations, electrochemical results, and characterizations such as HR-SEM, EDX, XPS, Raman and XRD spectra.

No. of Figures: 15

No. Tables: 6

Section 1: Materials Characterization

The crystal structure and phase purity were investigated using X-ray diffraction analysis (XRD) performed using Bruker D8 ADVANCE diffractometer equipped with a Cu K α radiation source. The FT-Raman spectroscopic analysis was executed using BRUKER RFS 27 MultiRAM FT Raman Spectrometer. A Perkin Elmer FT-IR spectrophotometer was used to obtain Fourier transform infrared spectra required to analyse the surface functional groups. The surface morphology was investigated using high resolution scanning electron microscopy (HRSEM) carried out using a HRSEM Thermo Scientific Apreo S equipped with energy dispersive X-ray (EDX) for verifying the elemental composition of the nanoparticles. The internal morphology was further analysed using high resolution transmission electron microscopy, HRTEM JEOL Japan, JEM-2100 Plus. The elemental composition and chemical state of the elements were confirmed using an Thermo Scientific X-ray photoelectron spectrometer equipped with an Al-K α micro-focused monochromator for performing X-ray photoelectron spectroscopy (XPS). The exact chemical composition was further analysed using Thermo Fisher iCAP RQ ICP-MS. The BET surface area and pore size was analysed using Quantachrome Instruments, Autosorb IQ series Nitrogen absorption/ desorption equipment.

Section 2: Electrochemical Characterizations for the three-electrode system

Electrocatalytic studies of these catalysts were done with the conventional three-electrode system. For the OER experiment we have used Carbon cloth (CC) as a counter electrode then the material was coated on Ni foam (4 \times 0.5 cm²). Hg/HgO electrode has been used as a reference electrode for OER in an alkaline medium. The polarization studies were carried out at a slow scan rate of 5 mV s⁻¹. 90% iR compensation was done manually from the Rs from EIS. All the potential in the LSV curve was converted into RHE by using the Nerst equation ($E_{\text{RHE}} = E_{\text{appl}} + E^0 + 0.059\text{pH}$). Whereas, E_{RHE} is the converted cell potential, E_{appl} is the applied potential, E^0 is the cell potential under standard conditions. Later, all the potential data have been converted concerning reversible hydrogen electrode (RHE). Overpotential is also calculated by using the formula $\eta = 1.23 - E_{\text{RHE}}$ V. Tafel slope talks about the relation between the applied over potential and current density in log scale and the corresponding plots is called as the Tafel plot. Tafel slope values are derived from the Butler-Volmer equation, which can be represented as $\eta = b \times \log(j) + a$ where, b , η , j , and a are represented as a Tafel slope,

overpotential, current density, and reaction constant, respectively. ECSA of the catalyst is directly proportional to the double-layer capacitance (C_{dl}) of the corresponding working electrode and described by the equation $ECSA = C_{dl}/C_s$. Whereas C_{dl} is double-layer capacitance and C_s is the capacitance of any flat electro surface ($0.04 \mu F cm^{-2}$). Calculation of overpotential is quite important to determine the activity of the catalyst, apart from that calculation of turnover frequency (TOF) is also necessary to find out the potentiality of a catalyst at a particular overpotential. TOF is simply defined as the number of moles of H_2/O_2 formed per unit time from a catalytic active site. The equation which is used to calculate the TOF value of a catalyst is given below, $TOF = (J \times N_A)/(n \times F \times \tau)$ where J is the current density at a certain overpotential, N_A is the Avogadro number, n is the number of electron transfers (OER $n = 4$ and HER $n = 2$), F is the faraday constant and τ is the number of active sites over the working electrode surface. The τ value can be calculated from the redox area curve, which is obtained from the CV at the highest possible scan rates. The chronoamperometry study was conducted using a three-electrode setup comprising a working electrode, reference electrode, and counter electrode. The electrochemical cell was assembled, and the working electrode surface was prepared as per experimental requirements. A fixed potential (1.47 V and -0.95 vs R.H.E for OER and HER, respectively) was applied using a potentiostat, and the resulting current was measured over a specified time duration. In the same way fixed cell potential of 1.6 V and 2 V towards TWS and AEMWE system. The collected data were then analyzed to determine relevant parameters. The electrochemical impedance studies were carried out in the frequency range of 1 Hz to 100 kHz with an overpotential of 350 mV for OER. EIS experimental data were analyzed and fitted using the Z-view software.

Calculation of Faradaic Efficiency (FE):

For the RRDE experiment, 4 mg of $\text{CuNd}_{1.7}\text{Gd}_{0.3}\text{O}_4$ catalyst was added to a solution containing 750 μL of H_2O , 200 μL of ethanol, and 50 μL of 5% Nafion solution. The above mixture was probe sonicated for 20 min to prepare a homogeneous catalyst ink. Later, 15 μL of homogeneous ink was drop-casted over the GC disk of RRDE set up with an effective surface area of $\approx 0.197 \text{ cm}^2$. The Pt ring was used with a constant potential of 0.3 V versus RHE to reduce the as-formed O^2 in situ. The FE was calculated from the ratio of the ring current to the disk using the following expression:

$$\text{FE} = I_{\text{ring}} / (I_{\text{disk}} \times N) \times 100$$

where, " I_{ring} " and " I_{disk} " are the ring and disk current density in mA cm^{-2} , respectively; " N " is the collection efficiency having a constant value of 0.284.

Section 3: Characterization techniques

Section 3a: XRD analysis

XRD analysis was carried out for the crystal structure investigation of the catalysts. Interestingly, a decrease in d-spacing was observed with increasing Gd concentration. This phenomenon can be attributed to the disparity in ionic radii between Nd^{3+} (1.109 Å) and Gd^{3+} (1.053 Å). The smaller Gd^{3+} ions likely restrict crystallite growth, leading to the observed contraction in d-spacing. Consistent with Vegard's law, the lattice parameters also exhibited a decrease with increasing Gd^{3+} concentration, reflecting the incorporation of the smaller cations.¹ The c/a ratio calculated is found to decrease linearly with increase in the dopant concentration. This suggests the compression of lattice along the c-axis in combination with a decrease in the overall volume.² Substituting rare-earth elements with those possessing higher atomic numbers leads to an enhancement in crystallite size. Conversely, increasing the dopant concentration induces a suppression of grain growth, resulting in a decrease in crystallite size.³

The lattice parameters, lattice strain, dislocation density and average crystallite size were calculated using the following equations (S1-S4),

$$\frac{1}{d^2} = \frac{h^2 + k^2}{a^2} + \frac{l^2}{c^2} \quad \dots(\text{S1})$$

Scherrer's equation

$$D = \frac{K \lambda}{\beta \cos(\theta)}$$

...(S2)

Stokes- Wilson formula

$$\varepsilon = \frac{\beta}{4 \tan \theta} \quad \dots(\text{S3})$$

$$\delta = \frac{1}{D^2} \quad \dots(\text{S4})$$

h, k, l - Miller's indices

a, b, c - unit cell lengths (a=b)

d - Interplanar distance

K - Shape factor (0.9)

λ - Wavelength of $\text{CuK}\alpha$ radiation (0.1554 nm)

β - Full width at half maximum of the XRD peaks

θ - Bragg angle of diffraction

Table S1. XRD details of CuNd_{1.7}Gd_{0.3}O₄ nanoparticles.

Catalyst	Diffraction angle (2θ) of (103) plane (degree)	d spacing of (103) plane (\AA)	Lattice Parameters				Lattice strain (ϵ) (10^{-3})	Dislocation density (δ) (lines/m ²) $\times 10^{14}$	Average Crystallite size (D) (nm)
			a (\AA)	c (\AA)	c/a	Volume = a x b x c (\AA^3)			
CNG (Conventional method)	31.60	2.830	3.941	12.202	3.0961	189.51	2.225	4.460	47.35
CNG (microwave method)	31.56	2.832	3.949	12.191	3.0867	190.17	2.821	6.338	39.72
0.1CNG	31.647	2.824	3.941	12.152	3.0832	188.79	2.849	5.128	44.15
0.3CNG	31.666	2.823	3.940	12.141	3.0810	188.52	2.474	5.477	42.72
0.5CNG	31.714	2.819	3.933	12.126	3.0825	187.65	3.046	8.455	34.39

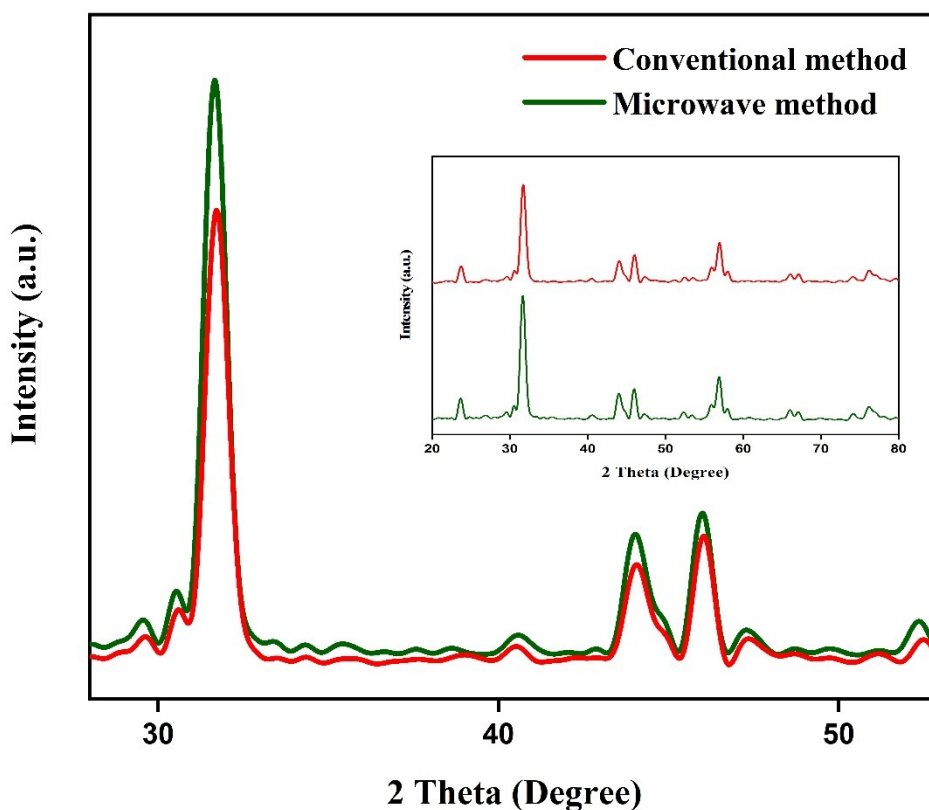


Fig. S1. XRD pattern of CuNd₂O₄ prepared by conventional method and microwave method.

Section 3b: FT-IR spectral analysis

The FT-IR peaks in **Fig. 2(b)**, portray identical functional group composition in the electrocatalysts. The peaks around 3430 and 1640 cm⁻¹ represent the stretching vibration of hydroxyl group and the bending vibrations of the associated water molecules, respectively.⁴ The C-O and O-C-O stretching modes due to the adsorbed carbonate species produce peaks oriented about 1030 and 1380 cm⁻¹.⁵ The absorption bands at low frequencies of 500- 600 cm⁻¹ are attributed to the Cu-O bond.⁶ The stretching vibrations of Nd-O produce peaks at 780 and 530 cm⁻¹.⁷ Gd-O stretching also produces peaks around 500 cm⁻¹.⁸ Hence incorporation of Gd might cause the minor shift in the M-O IR absorption bands.

Section 3c: HR-SEM analysis

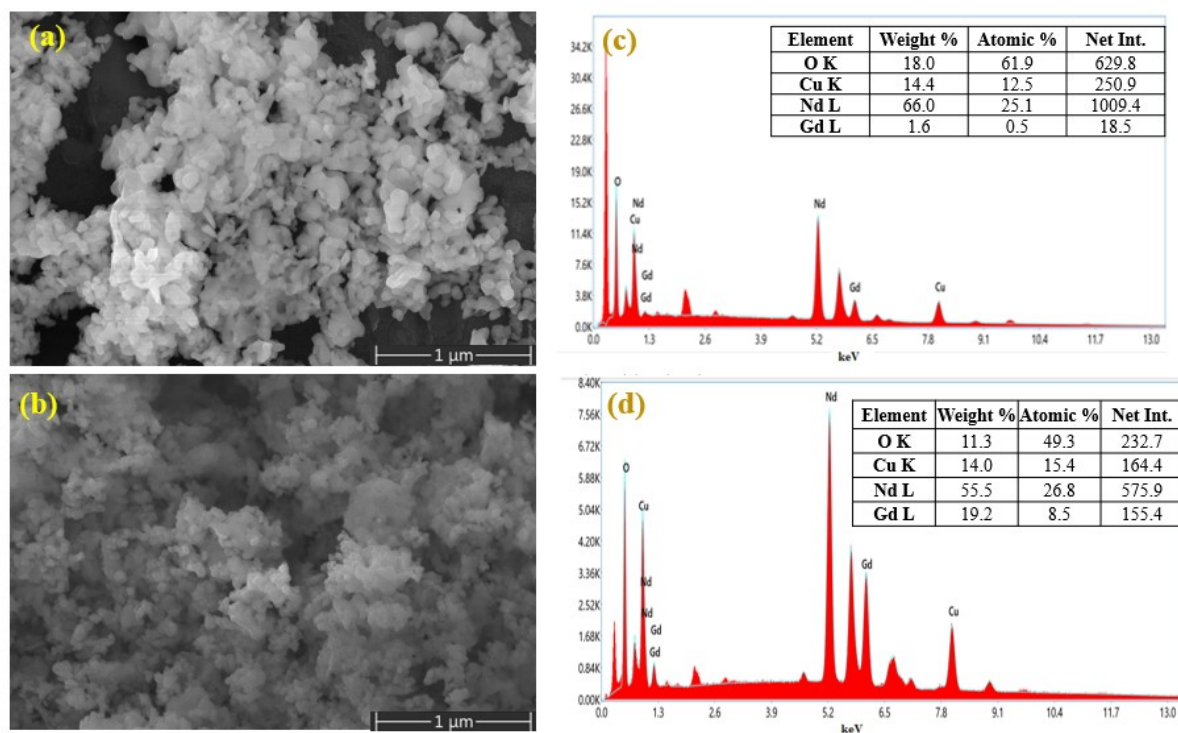


Fig. S2. (a, b) HR-SEM images of $\text{CuNd}_{1.9}\text{Gd}_{0.1}\text{O}_4$ and $\text{CuNd}_{1.5}\text{Gd}_{0.5}\text{O}_4$ and (c, d) their corresponding EDX analysis.

Section 3d: XPS analysis

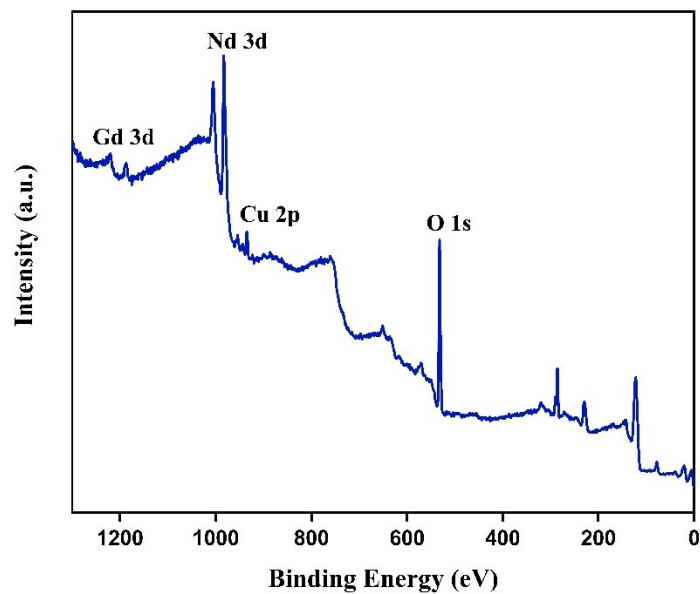


Fig. S3. XPS Survey Spectrum of $\text{CuNd}_{1.7}\text{Gd}_{0.3}\text{O}_4$.

Table S2. Elemental composition of $\text{CuNd}_{1.7}\text{Gd}_{0.3}\text{O}_4$ examined by XPS analysis.

Name	Peak BE	Area (P) CPS eV	Atomic %
O 1s	531.97	2383417.32	82.32
Cu 2p	934.73	669727.42	3.76
Nd 3d	982.46	2835580.48	10.91
Gd 3d	1220.02	1049283.07	3.01

Section 3e: ICP-MS analysis

Table S3. Concentration of various metallic components from ICP-MS analysis.

S.No.	Electrocatalys t	Concentration (ppm)		
		Cu	Nd	Gd
1.	CuNd_2O_4	7.23	13.96	-
2.	$\text{CuNd}_{1.7}\text{Gd}_{0.3}\text{O}_4$	6.89	11.10	1.93

Section 4: Electrocatalytic OER study in alkaline medium.

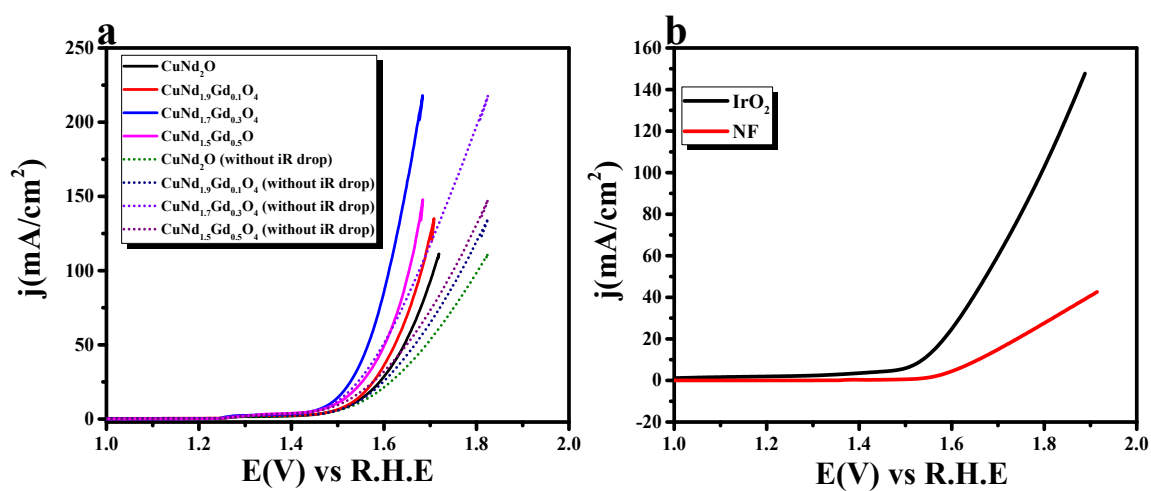


Fig. S4. (a) LSV polarization outcomes obtained with a scan rate of 5 mV s⁻¹ with and without iR-correction, and (b) LSV polarization outcomes obtained with a scan rate of 5 mV s⁻¹ for IrO₂ and NF.

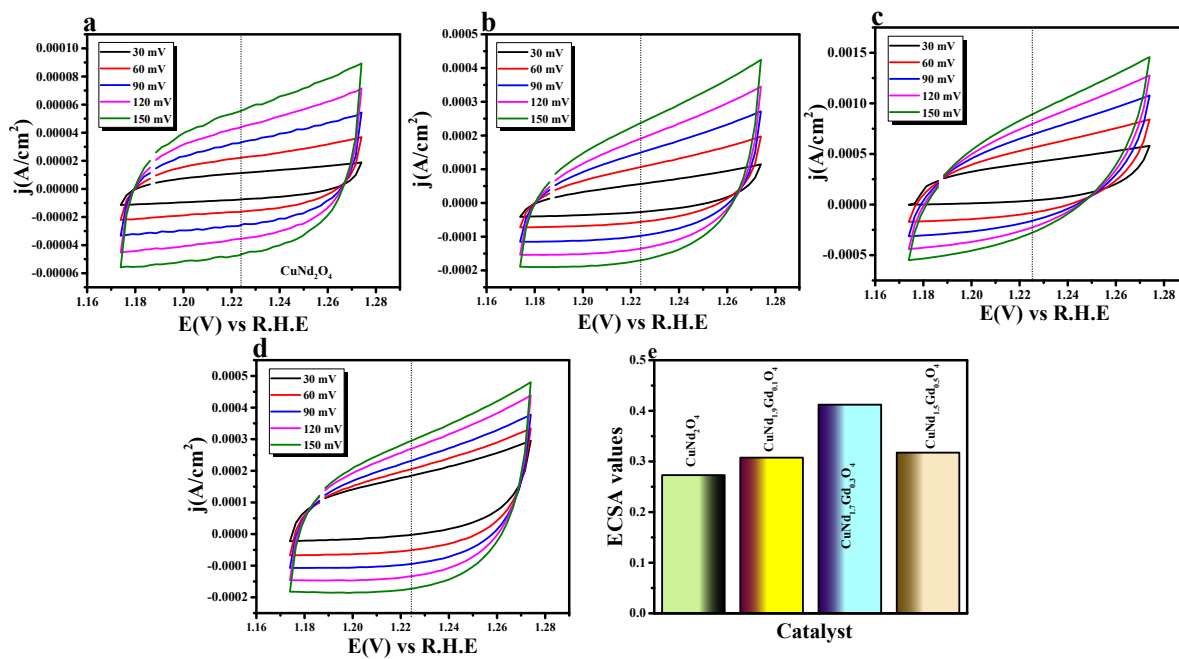


Fig. S5. (a-d) scan rate-dependent CV curves obtained for calculating the C_{dl} value in the non-faradaic region of 1.12-1.23 V vs R.H.E and (e) Calculated ECSA values of all prepared electrode material.

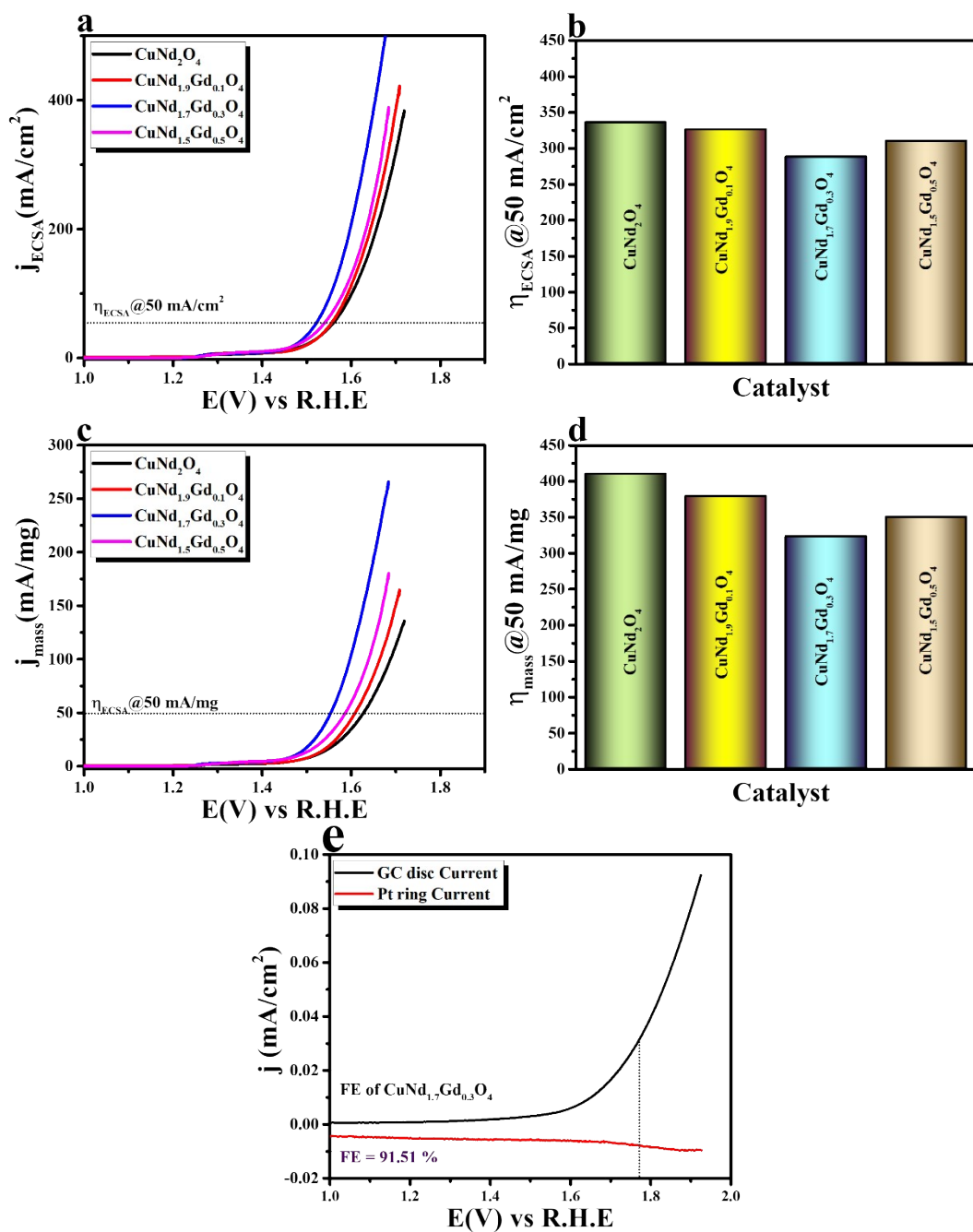


Fig. S6. (a) ECSA-normalized polarization curve; (b) bar diagram of ECSA-normalized overpotential values @50 mA cm⁻² current density; (c) mass-normalized polarization curve (d) bar diagram of mass-normalized overpotential values @50 mA cm⁻² current density and (e) Faradaic efficiency (FE) of the CuNd_{1.7}Gd_{0.3}O₄ electrocatalyst for OER in 1 M KOH solution.

Table S4. Comparison of recently reported OER catalysts for alkaline electrolysis.

Sl.No.	Electrocatalyst	Substrate	Overpotential (mV)	Electrolyte (M)	Current density (mA cm ⁻²)	References
1.	CuNd _{1.7} Gd _{0.3} O ₄	Nickel foam	243	1 M KOH	10	This work
2.	CeO ₂ -Y ₂ O ₃ -Nd ₂ O ₃ /rGO	Nickel foam	272	1 M KOH	10	⁹
3.	Nd-MnO	Nickel foam	394	1 M KOH	10	¹⁰
4.	CeNdS/C ₆₀	Nickel foam	346	1 M KOH	10	¹¹
5.	Nd ₂ O ₃ @C	Stainless steel	299	1 M KOH	10	¹²
6.	Gd ₂ NiMnO ₆	Stainless steel	292	1 M KOH	10	¹³
7.	CuO/CuS	Nickel foam	270	1 M KOH	10	¹⁴
8.	CuNCs@4MP	Graphitic sheet	280	1M KOH	10	¹⁵
9.	AgNW@Cu ₂ O	Copper sheet	409	1 M KOH	10	¹⁶
10.	NdFe _{1-x} Ni _x O ₃	Nickel plate	310	1 M KOH	10	¹⁷

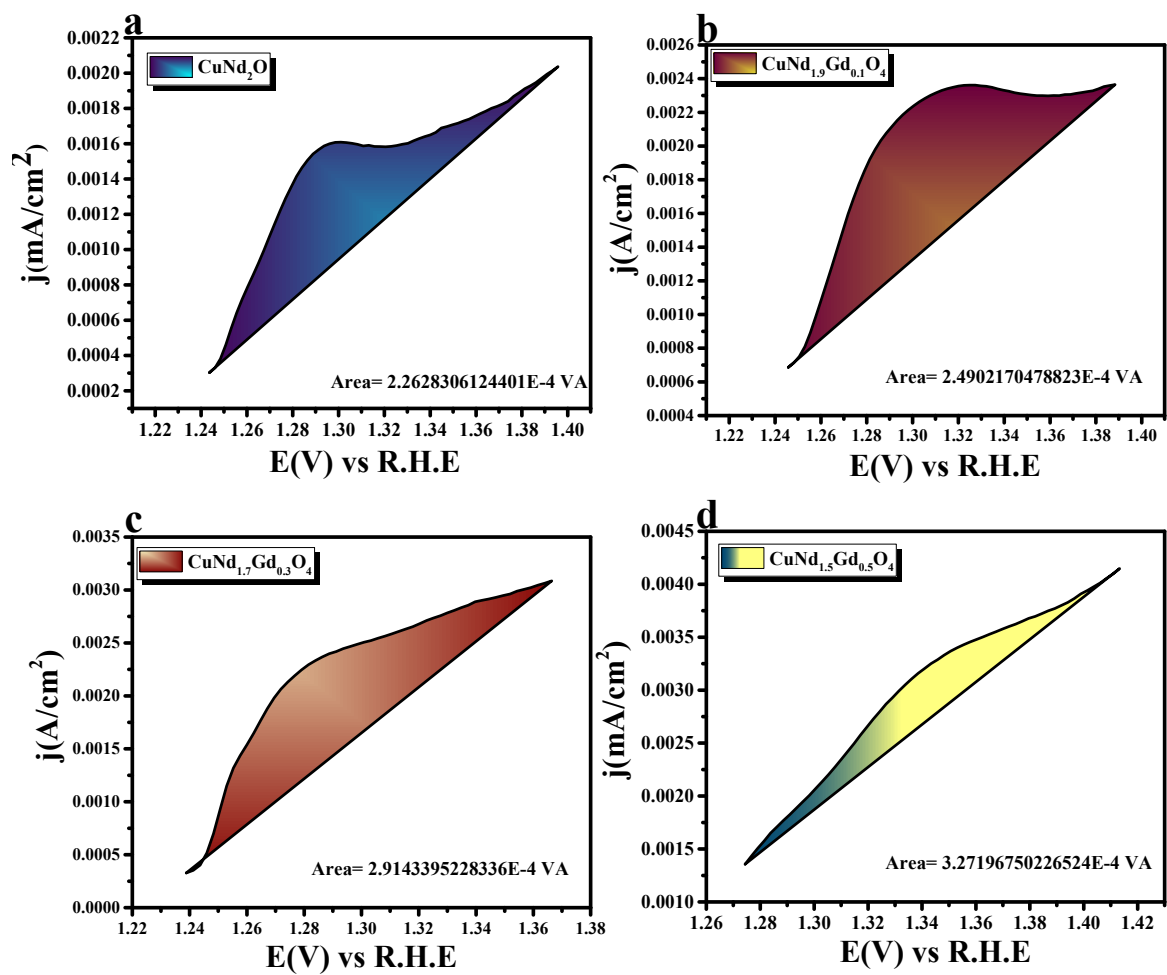


Fig. S7. (a-d) are the reduction surface area for the prepared electrode materials.

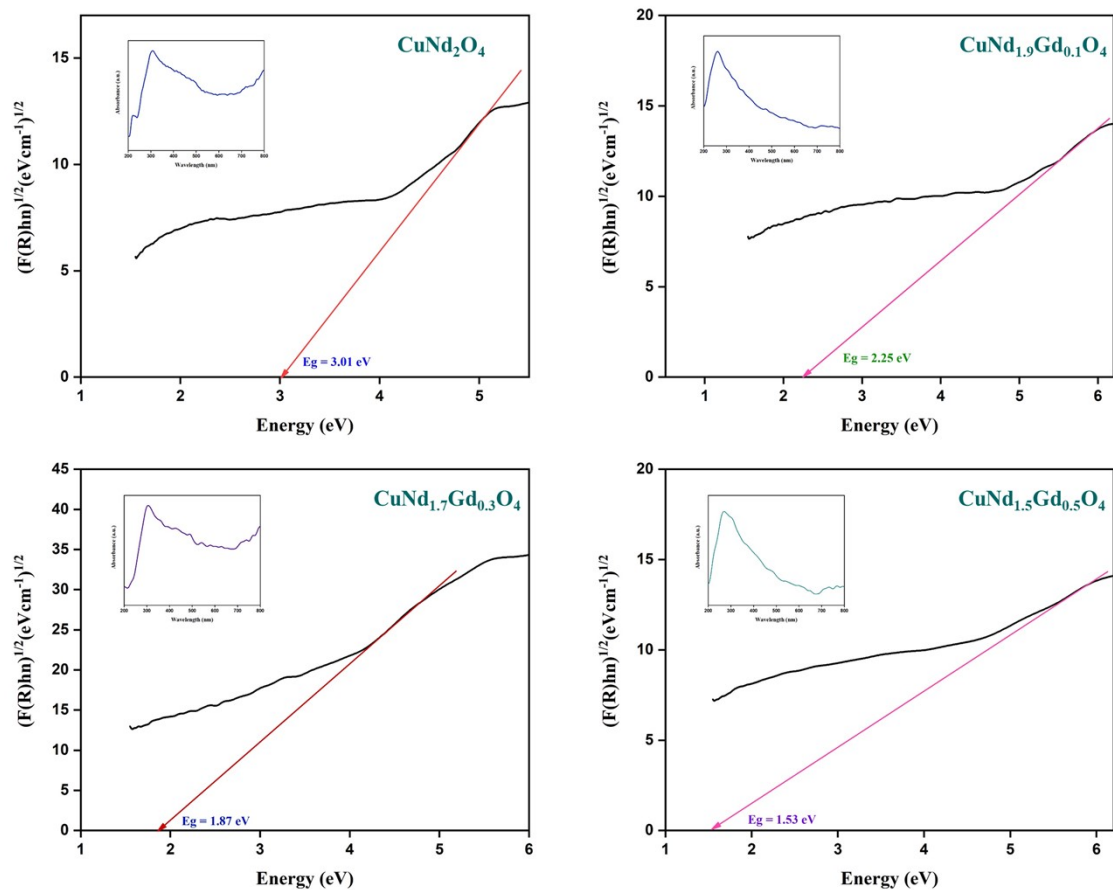


Fig. S8. Kubelka-Munk plots of $\text{CuNd}_{(2-x)}\text{Gd}_x\text{O}_4$ and inset is their absorbance spectra.

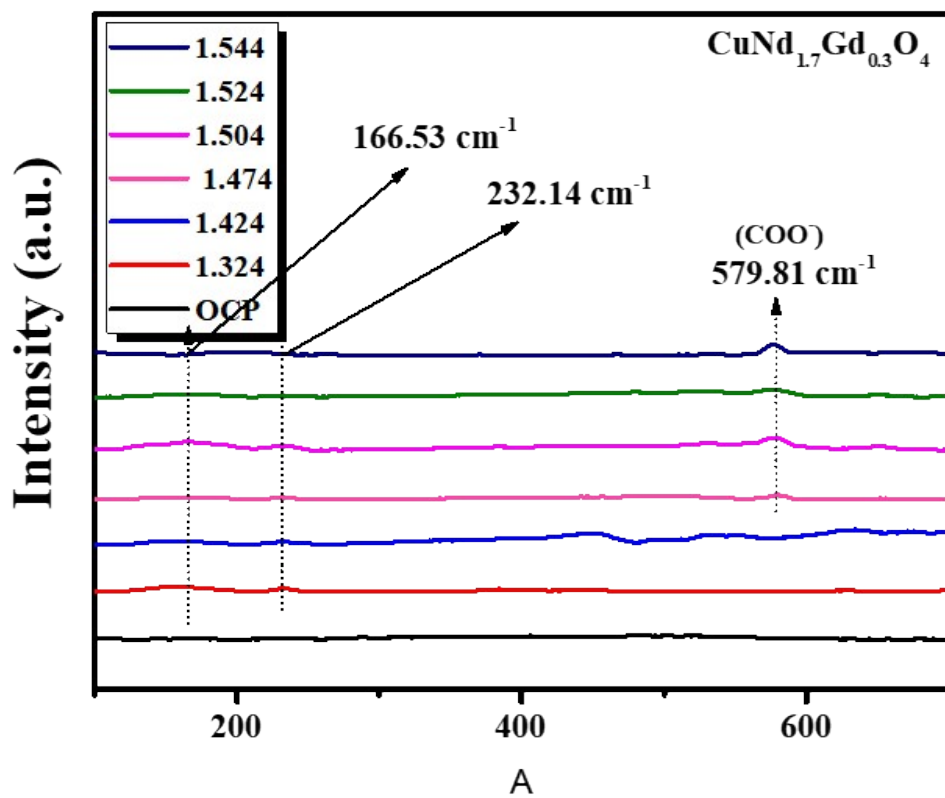


Fig. S9. in situ/operando Raman spectra of $\text{CuNd}_{1.7}\text{Gd}_{0.3}\text{O}_4$ electrodes in 1 M KOH solution.

Section 5: Electrocatalytic OER study in alkaline medium

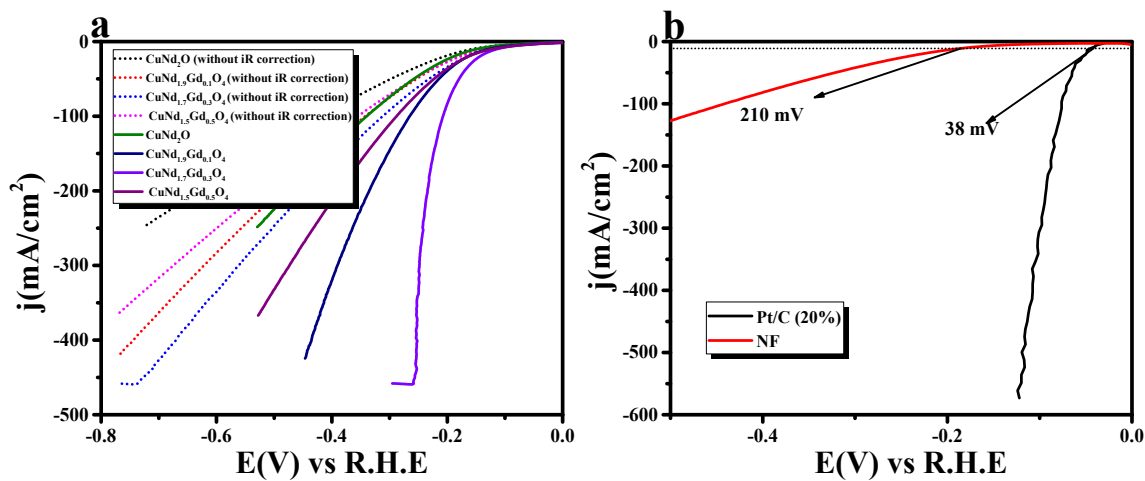


Fig. S10. (a) LSV polarization outcomes were obtained with a scan rate of 5 mV s⁻¹ with and without iR -correction, and (b) LSV polarization outcomes were obtained with a scan rate of 5 mV s⁻¹ for Pt/C and NF.

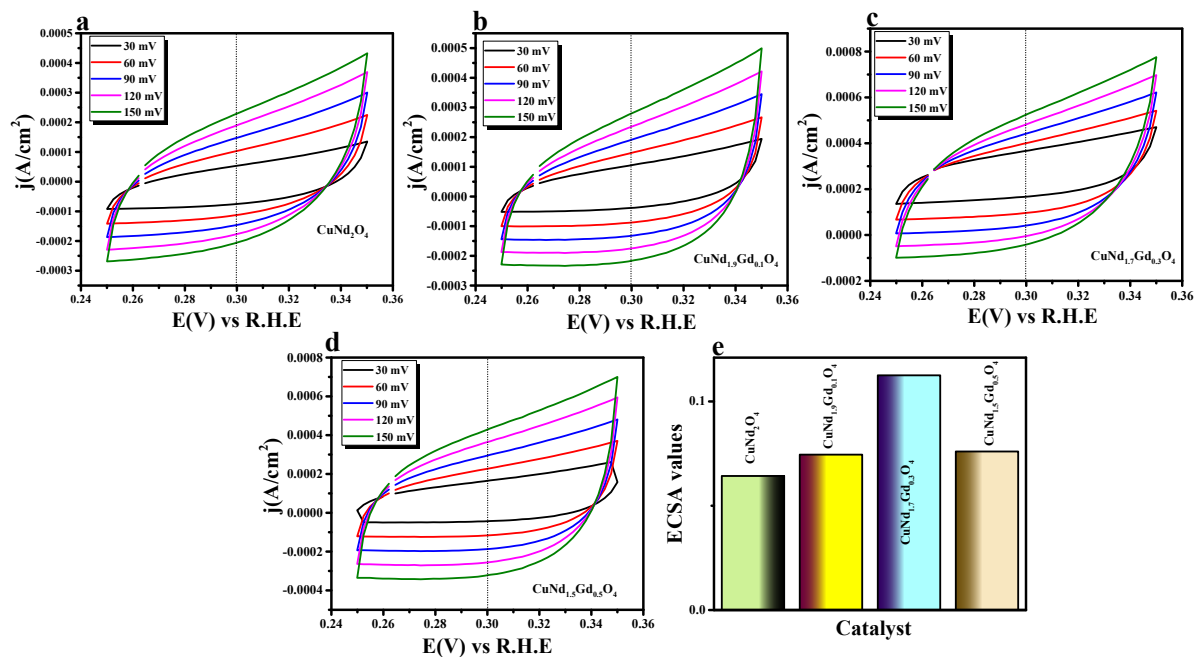


Fig. S11. (a-d) scan rate-dependent CV curves obtained for calculating the C_{dl} value in the non-faradaic region of 0.25-0.35 V vs R.H.E and (e) Calculated ECSA values of all prepared electrode material.

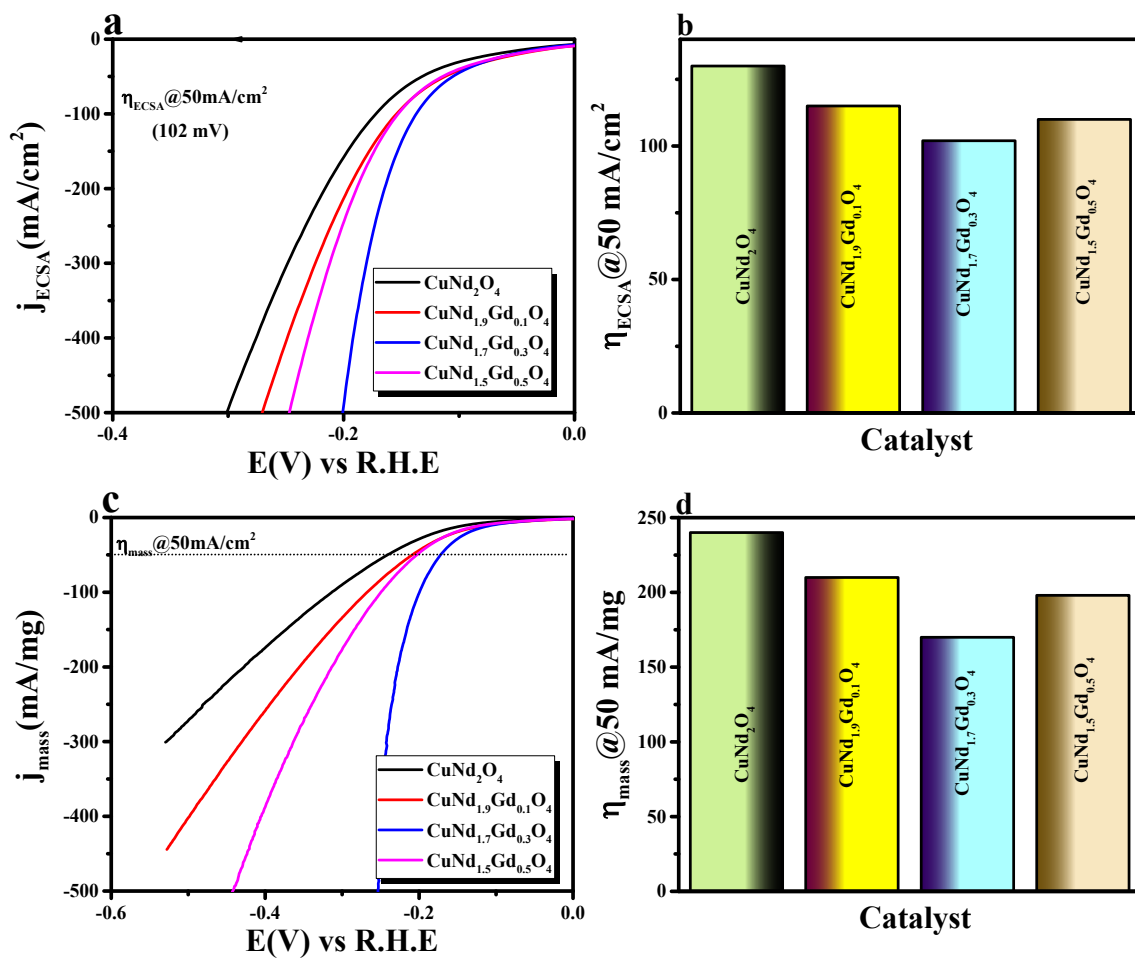


Fig. S12. (a) ECSA-normalized polarization curve; (b) bar diagram of ECSA-normalized overpotential values @50 mA cm⁻² current density; (c) mass-normalized polarization curve and (d) bar diagram of mass-normalized overpotential values @50 mA cm⁻² current density.

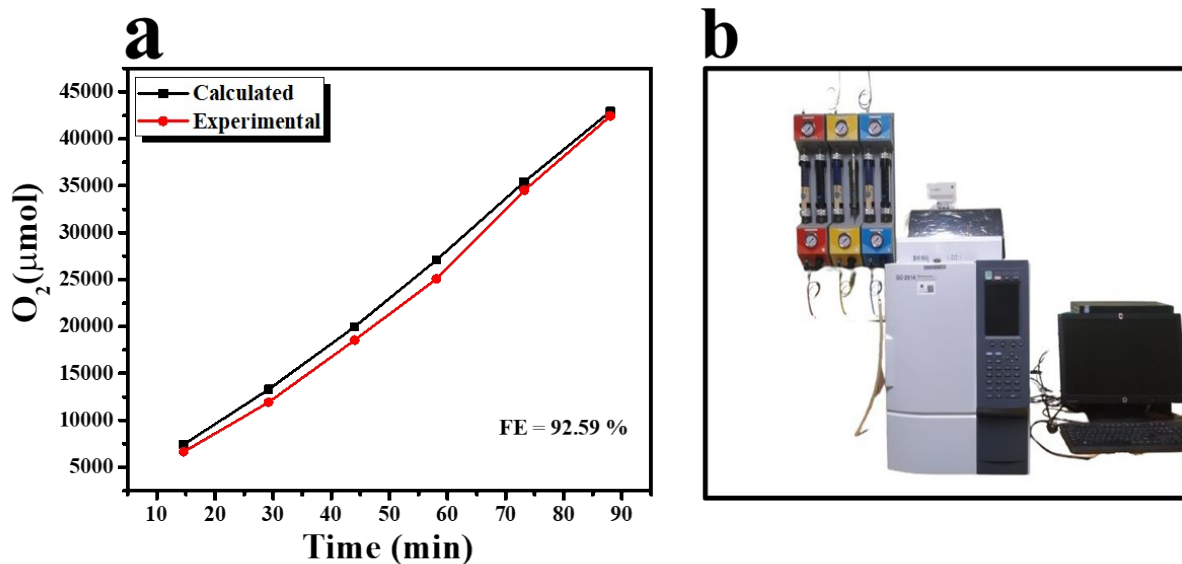


Fig. S13. (a) Quantitative analysis of produced O_2 in $CuNd_{1.7}Gd_{0.3}O_4$ with different time intervals measured via gas-chromatography. Faradaic efficiency plot for $CuNd_{1.7}Gd_{0.3}O_4$ by comparing the measured and theoretically evolving gas through GC-MS and (b) Experimental set-up for chronoamperometric study to quantify the evolving gas and Typical GC-MS features for $CuNd_{1.7}Gd_{0.3}O_4$.

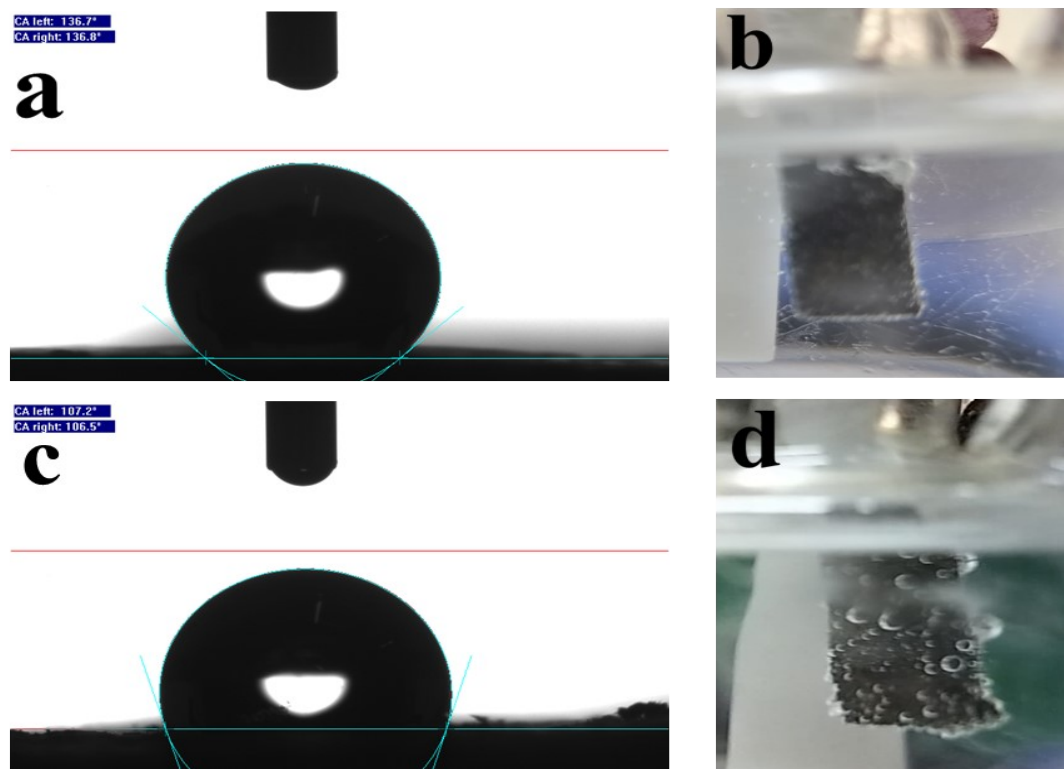


Fig. S14. Study of bubble release dynamics. The contact angle of air bubble with a) CuNd_{1.7}Gd_{0.3}O₄, c) CuNd₂O₄, and b, d) snapshot of CuNd_{1.7}Gd_{0.3}O₄ and CuNd₂O₄ electrodes operating at lower (25 mA cm⁻²). For Checking this Bubble dynamics we have used Carbon Fiber in order to get clear snaps of the particular reaction.

Table S5. Comparison of recently reported HER catalysts for alkaline electrolysis.

Sl.No.	Electrocatalyst	Substrate	Overpotential (mV)	Electrolyte (M)	Current density (mA cm ⁻²)	References
1.	CuNd _{1.7} Gd _{0.3} O ₄	Nickel Foam	118	1 M KOH	10	This work
2.	CeO ₂ -Y ₂ O ₃ -Nd ₂ O ₃ /rGO	Nickel foam	303	1 M KOH	10	⁹
3.	Co _{10%} -CuV	glassy carbon	176	1 M KOH	10	¹⁸
4.	Cu _{1+n} /BDNC	Nickel foam	216	1 M KOH	10	¹⁹
5.	Cu ₂ CoSnS ₄	Whatman filter paper	233 / 310 / 261	0.5 M H ₂ SO ₄ / 1 M KOH / 1 M PBS	10	²⁰
6.	Cu _{0.35} Co _{2.65} O ₄ NPs@N-RGO	glassy carbon	170	1 M KOH	10	²¹
7.	Cu ₃ P/Cu ₂ Se	copper foam	166	1 M KOH	10	²²
8.	[Gd-Ho-Dy]: ZrO ₂	Nickel foam	134	0.5 M H ₂ SO ₄	10	²³
9.	Co _{0.45} Fe _{0.45} Ni _{0.9} -MOF	Nickel foam	164	1 M KOH	10	²⁴
10.	Co-MOF/CNF	Nickel foam	193	1 M KOH	10	²⁵
11.	ZnTi _{1-x} Zr _x O ₃	Nickel foam	165	1 M KOH	10	²⁶

Section 6: Post OER and HER characterizations.

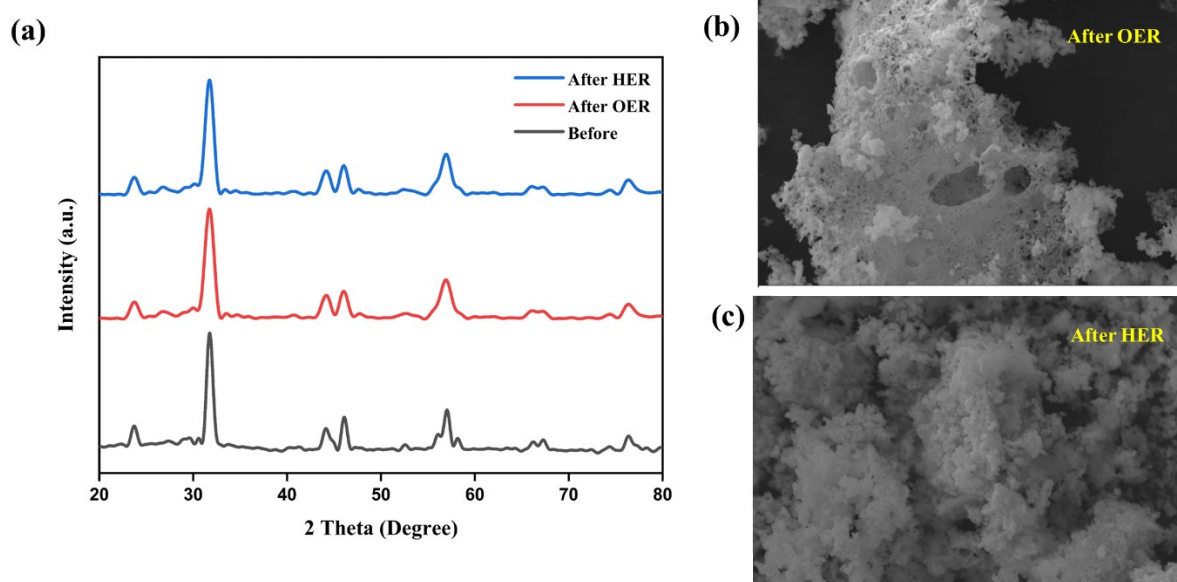


Fig. S15. (a) XRD pattern of $\text{CuNd}_{1.7}\text{Gd}_{0.3}\text{O}_4$ and SEM images of $\text{CuNd}_{1.7}\text{Gd}_{0.3}\text{O}_4$ after (b) OER and (c) HER.

Section 7: Electrocatalytic total water splitting in alkaline media.

Table S6: Comparison of recently reported TWS catalysts for alkaline electrolysis.

Sl.No.	Electrocatalyst	Substrate	Voltage (V)	Electrolyte (M)	Current density (mA cm ⁻²)	References
1.	CuNd_{1.7}Gd_{0.3}O₄	Nickel foam	1.62	1 M KOH	10	This work
2.	Faceted CuMn ₂ O ₄	Copper foam	1.9	1 M KOH	10	27
3.	Fe _x Ni _y /CeO ₂ /NC1	Nickel foam	1.70	1 M KOH	10	28
4.	Ni ₃ (NO ₃) ₂ (OH) ₄ /CeO ₂	Nickel foam	1.64	1 M KOH	10	29
5.	LaNi ₅	Nickel foam	1.68	1 M KOH	10	30
6.	Ru-doped CuO/MoS ₂	Nickel foil	1.68	1 M KOH	10	31
7.	Mo-CoP	Glassy carbon	1.7	1 M KOH	10	32
8.	Co-BTC MOF	Carbon cloth	2.03	1 M KOH	10	33

References

- 1 H. Yao, X. Ning, H. Zhao, A. Hao and M. Ismail, *ACS Omega*, 2021, 6, 6305–6311.
- 2 G. Singh, R. Thangaraj and R. C. Singh, *Ceram Int*, 2016, 42, 4323–4332.
- 3 C. Aziz and B. Azhdar, *J Magn Magn Mater*, 2022, 542, 168577.
- 4 S. Nagappan, R. Jayan, N. Rajagopal, A. V Krishnan, M. M. Islam and S. Kundu, *Small*, , DOI:10.1002/sml.202403908.
- 5 E. D. Sherly, J. J. Vijaya and L. J. Kennedy, *Chinese Journal of Catalysis*, 2015, 36, 1263–1272.
- 6 S. Sukumar, A. Rudrasenan and D. Padmanabhan Nambiar, *ACS Omega*, 2020, 5, 1040–1051.
- 7 M. Sundrarajan and V. Muthulakshmi, *J Environ Chem Eng*, 2021, 9, 104716.
- 8 M. J. Paul, R. Suresh, K. T. Valavan, R. Marnadu, M. Vidhya, N. Ahmad, A. M. Alshehri and S. Gedi, *J Alloys Compd*, 2021, 886, 161196.
- 9 T. Munawar, A. Bashir, K. M. Batoo, F. Mukhtar, M. S. Nadeem, S. Hussain, S. Manzoor, M. N. Ashiq, S. A. Khan, M. Koc and F. Iqbal, *Journal of the Korean Ceramic Society*, 2024, 61, 693–712.
- 10 M. U. Nisa, K. Jabbour, S. Manzoor, K. F. Fawy, A. G. Abid, F. Hussain, S. A. M. Abdelmohsen, M. M. Alanazi and M. N. Ashiq, *Journal of Electroanalytical Chemistry*, 2023, 945, 117705.
- 11 T. Munawar, A. Bashir, M. S. Nadeem, F. Mukhtar, S. Manzoor, M. N. Ashiq, S. A. Khan, M. Koc and F. Iqbal, *Energy & Fuels*, 2023, 37, 1370–1386.
- 12 T. Munawar, A. Bashir, M. S. Nadeem, F. Mukhtar, S. Manzoor, M. N. Ashiq, S. A. Khan, M. Koc and F. Iqbal, *Fuel*, 2024, 355, 129485.
- 13 K. P. Shinde, H. S. Chavan, A. S. Salunke, J. Oh, A. T. Aqueel Ahmed, N. K. Shrestha, H. Im, J. Park and A. I. Inamdar, *Nanomaterials*, 2023, 13, 3076.
- 14 N. A. Khan, I. Ahmad, N. Rashid, S. Hussain, R. Zairov, M. Alsaiani, A. S. Alkorbi, Z. Ullah, Hafiz urRehman and M. F. Nazar, *Int J Hydrogen Energy*, 2023, 48, 31142–31151.
- 15 V. Saini, Krishankant, S. Choudhary, A. Gaur, S. Banerjee, V. Bagchi and V. Venkatesh, *J Mater Chem A Mater*, 2023, 11, 24754–24763.
- 16 S. Battiato, A. Sekkat, C. S. Velasquez, A. L. Pellegrino, D. Bellet, A. Terrasi, S. Mirabella and D. Muñoz-Rojas, *Nanoscale Adv*, 2024, 6, 4426–4433.
- 17 Y. Khreif, M. Omari and S. Makhloufi, *Inorganica Chim Acta*, 2024, 566, 122028.
- 18 V. Tripathi, S. Jain, D. Kabra, L. S. Panchakarla and A. Dutta, *Nanoscale Adv*, 2023, 5, 237–246.

- 19 W. Zhang, R. Liu, Z. Fan, H. Wen, Y. Chen, R. Lin, Y. Zhu, X. Yang and Z. Chen, *Inorg Chem Front*, 2023, 10, 443–453.
- 20 K. K. Joshi, P. M. Pataniya, G. R. Bhadu and C. K. Sumesh, *Int J Hydrogen Energy*, 2024, 49, 829–842.
- 21 T. Niyitanga and H. Kim, *J Power Sources*, 2023, 580, 233383.
- 22 C. An, Y. Wang, R. Huang, Y. Li, C. Wang, S. Wu, L. Gao, C. Zhu, Q. Deng and N. Hu, *Colloids Surf A Physicochem Eng Asp*, 2023, 667, 131360.
- 23 S. B. Jaffri, K. S. Ahmad, I. Abrahams and M. A. Habila, *Opt Mater (Amst)*, 2024, 154, 115712.
- 24 Y. Liu, P. Li, Z. Wang and L. Gao, *Materials*, 2024, 17, 2195.
- 25 P. Suresh, U. Rajaji, A. Natarajan, K. Rajagopal, A. A. Alothman and T.-Y. Liu, *Chem Phys Lett*, 2024, 847, 141371.
- 26 M. K. Adak, D. Mondal, U. Mahato, H. K. Basak, S. Mandal, A. Das, B. Chakraborty and D. Dhak, *Int J Hydrogen Energy*, 2023, 48, 39910–39929.
- 27 B. J. Rani, A. Sivanantham, T. S. Shridharan, T. Runfa and I. S. Cho, *J Mater Chem A Mater*, 2022, 10, 17710–17720.
- 28 L. Chen, H. Jang, M. G. Kim, Q. Qin, X. Liu and J. Cho, *Inorg Chem Front*, 2020, 7, 470–476.
- 29 X. Zhang, Y. Qiu, Q. Li, F. Liu, X. Ji and J. Liu, *Int J Hydrogen Energy*, 2022, 47, 23221–23229.
- 30 Y. Wu, Y. Liu, K. Liu, L. Wang, L. Zhang, D. Wang, Z. Chai and W. Shi, *Green Energy & Environment*, 2022, 7, 799–806.
- 31 A. Maiti and S. K. Srivastava, *ACS Appl Nano Mater*, 2021, 4, 7675–7685.
- 32 L. Li, Y. Guo, X. Wang, X. Liu and Y. Lu, *Langmuir*, 2021, 37, 5986–5992.
- 33 S. Naik Shreyanka, J. Theerthagiri, S. J. Lee, Y. Yu and M. Y. Choi, *Chemical Engineering Journal*, 2022, 446, 137045.